RESEARCH ARTICLE

Development and application of a novel tumor habitat analysis technique based on dynamical modeling

Jack B Stevens[1] | Jihyeon Je[2] | Breylon A Riley[1] | Yvonne M Mowery[3,4,5] | David M Brizel[3,4] | Jian-Guo Liu[6,7] | Chunhao Wang[1,3] | Kyle J Lafata[1,2,3,6,8]

[1]Medical Physics Graduate Program, Duke University, Durham, North Carolina, USA

[2]Department of Electrical and Computer Engineering, Duke University Pratt School of Engineering, Durham, North Carolina, USA

[3]Department of Radiation Oncology, Duke University School of Medicine, Durham, North Carolina, USA

[4]Department of Head and Neck Surgery & Communication Sciences, Duke University School of Medicine, Durham, North Carolina, USA

[5]Department of Radiation Oncology, UPMC Hillman Cancer Center/University of Pittsburgh, Pittsburgh, Pennsylvania, USA

[6]Department of Mathematics, Duke University, Durham, North Carolina, USA

[7]Department of Physics, Duke University, Durham, North Carolina, USA

[8]Department of Radiology, Duke University School of Medicine, Durham, North Carolina, USA

Correspondence
Kyle J Lafata, 2424 Erwin Rd Suit 301, Durham, NC 27705, USA.
Email: kyle.lafata@duke.edu

Abstract

Background: Oropharyngeal cancer (OPC) exhibits varying responses to chemoradiation therapy, making treatment outcome prediction challenging. Traditional imaging-based methods often fail to capture the spatial heterogeneity within tumors, which influences treatment resistance and disease progression. Advances in modeling techniques allow for more nuanced analysis of this heterogeneity, identifying distinct tumor regions, or habitats, that drive patient outcomes.

Purpose: To interrogate the association between treatment-induced changes in spatial heterogeneity and chemoradiation resistance of oropharyngeal cancer (OPC) based on a novel tumor habitat analysis.

Methods: A mathematical model was used to estimate tumor time dynamics of patients with OPC based on the applied analysis of partial differential equations. The position and momentum of each voxel was propagated according to Fokker-Planck dynamics, that is, a common model in statistical mechanics. The boundary conditions of the Fokker-Planck equation were solved based on pre- and intra-treatment (i.e., after 2 weeks of therapy) ^{18}F-FDG-PET SUV images of patients ($n = 56$) undergoing definitive (chemo)radiation for OPC as part of a previously conducted prospective clinical trial. Tumor-specific time dynamics, measured based on the solution of the Fokker-Planck equation, were generated for each patient. Tumor habitats (i.e., non-overlapping subregions of the primary tumor) were identified by measuring vector similarity in voxel-level time dynamics through a fuzzy c-means clustering algorithm. The robustness of our habitat construction method was quantified using a mean silhouette metric to measure intra-habitat variability. Fifty-four habitat-specific radiomic texture features were extracted from pre-treatment SUV images and normalized by habitat volume. Univariate Kaplan-Meier analyses were implemented as a feature selection method, where statistically significant features ($p < 0.05$, log-rank) were used to construct a multivariate Cox proportional-hazards model. Parameters from the resulting Cox model were then used to construct a risk score for each patient, based on habitat-specific radiomic expression. The patient cohort was stratified by median risk score value and association with recurrence-free survival (RFS) was evaluated via log-rank tests.

Results: Dynamic tumor habitat analysis partitioned the gross disease of each patient into three spatial subregions. Voxels within each habitat suggested differential response rates in different compartments of the tumor. The minimum mean silhouette value was 0.57 and maximum mean silhouette value was 0.8, where values above 0.7 indicated strong intra-habitat consistency and values between 0.5 and 0.7 indicated reasonable intra-habitat consistency. Nine radiomic texture features (three GLRLM, two GLCOM, and three GLSZM) and

SUVmax were found to be prognostically significant and were used to build the multivariate Cox model. The resulting risk score was associated with RFS ($p = 0.032$). By contrast, potential confounding factors (primary tumor volume and mean SUV) were not significantly associated with RFS ($p = 0.286$ and $p = 0.231$, respectively).

Conclusion: We interrogated spatial heterogeneity of oropharyngeal tumors through the application of a novel algorithm to identify spatial habitats on SUV images. Our habitat construction technique was shown to be robust and habitat-specific feature spaces revealed distinct underlying radiomic expression patterns. Radiomic features were extracted from dynamic habitats and used to build a risk score which demonstrated prognostic value.

1 | INTRODUCTION

Oropharyngeal cancers (OPC) are a major contributor to the number of overall cancer diagnoses and deaths in the United States.[1] Whilst therapeutic strategies for the treatment of OPC are multimodal, including surgery and/or neoadjuvant chemoradiation, normal tissue toxicities remain a key challenge and often negatively impact quality of life.[2] Adaptive therapy has emerged as a promising technique, whereby dose and/or treatment volumes are modified throughout the course of therapy, for example deintensification[3] of dose for early responding HPV-positive OPC tumors.[4–6] Imaging may provide important prognostic information that can guide adaptive therapies. For example, ^{18}F-FDG PET images can quantify the underlying metabolic properties of OPC tumors[7–9] as a surrogate biomarker of adaptive intervention. Recent work has also suggested that intra-treatment ^{18}F-FDG-PET imaging, where patients are additionally imaged *during* the chemoradiation regiment, may provide further prognostic information to guide adaptive therapy.[10,11]

Spatial heterogeneity of tumor metabolism measured with ^{18}F-FDG-PET has been identified as an important feature associated with patient outcomes.[12–16] Prior work has suggested that heterogeneity in tumor metabolism is correlated with hypoxic tumor sub-regions,[17] which has been further investigated using targeted hypoxia radiotracers.[14,18,19] Spatial heterogeneity in OPC tumors is primarily characterized either by aggregate metrics, such as maximum standardised uptake value (SUVmax), or high-throughput computational techniques, such as radiomics. Tumor SUVmax has been extensively studied as a potential prognostic biomarker and has been linked to poor patient outcomes.[11,20–25] However, recent studies argue that reducing complex tumor biology to a single number is an oversimplification[26] and that the association between SUV-based parameters and patient outcomes is not robust.[27,28] As a result, high-throughput radiomic techniques have increasingly been applied to derive more complex features that could be used to adapt treatment strategies. For example, pre-treatment ^{18}F-FDG-PET radiomics have been used to predict clinically relevant endpoints for OPC, such as locoregional recurrence,[29] overall survival,[30] and normal tissue toxicities.[31] Still, the scientific results of these studies have been mixed, with some highlighting predictive value[32–34] and others finding no such value.[10,35]

Data assimilation of radiomic expression with deterministic, mathematical models may enhance the fidelity of purely data-driven radiomics research.[10,36–39] These models often address key limitations in quantitative imaging research and offer the potential for deeper and more nuanced analysis of radiomic feature expression. For example, novel clustering algorithms (based on mathematical models commonly used in statistical mechanics) have been developed to partition OPC patients based only on ^{18}F-FDG-PET radiomic expression patterns.[37] Likewise, deterministic models have also been used to link the biological effect of radiation dose to deep learning outcome predictions for OPC patients.[36] Finally, these approaches also add utility to study time interval analyses, that is, characterization of image time evolution to interrogate the progression of disease between different timepoints.[38] Collectively, these approaches can quantify changes in spatial heterogeneity of tumors during treatment by modeling the time dynamics of the tumor and incorporating that information into the radiomic analysis.

In this work, we propose a novel approach to construct spatial tumor habitats based on the time evolution of metabolic uptake measured on ^{18}F-FDG-PET SUV images of OPC patients. While previous studies rely on image thresholding or static clustering methods to create spatial tumor habitats,[15,16,40–45] our habitat approach incorporates time dynamics into the problem, allowing for a more detailed characterisation of underlying spatial heterogeneity in response to treatment. Our implementation is based on an underlying mathematical framework to model tumor-specific time dynamics parameterized by clinical PET images. We use a fuzzy clustering algorithm to construct spatial-temporal habitats and demonstrate that habitat-specific radiomic features are associated with patient outcomes. Interrogation of underlying spatial-temporal heterogeneity

in oropharyngeal tumors will likely enable robust and biologically informed studies that connect the disease phenotype to patient outcomes.

2 | METHODS

2.1 | Patients, treatment, and image acquisition

We developed and evaluated our dynamic tumor habitat approach based on patients enrolled on a prospective, single-institution clinical trial (NCT01908504) conducted at Duke University Medical Center.[11] Specifically, we considered patients that underwent curative radiotherapy for oropharyngeal cancer (OPC). Patients were prescribed a course of intensity-modulated radiation therapy (IMRT) according to standard clinical practice, and the majority received concurrent chemotherapy. The dose prescription was either 70 Gy in 35 fractions, or 67.5 Gy in 30 fractions, with the sequential boost strategy. Fifty-six patients with confirmed OPC were studied. All patients had known primary disease, no prior surgical removal or resection of the primary tumor, no prior chemotherapy, and single primary tumors. Follow-up included fiberoptic laryngoscopy, additional imaging as needed, and biopsies of suspicious lesions. Recurrence-free survival (RFS) was the primary clinical endpoint and defined as the time from conclusion of radiation treatment to disease recurrence. Patients lost to follow-up were censored at the last date of follow-up. The full patient characteristics are shown in Table S1.

Each patient received two ^{18}F-FDG-PET/CT scans, one prior to radiation treatment and one intra-treatment, that is, after 2 weeks (20 Gy) of therapy. Scanner type, imaging protocols, and acquisition parameters were consistent across all patients. Primary gross tumor segmentation was performed by a radiation oncologist on CT images and subsequently transferred to the PET images. Images were interpolated to an isotropic resolution of 1.17 mm and re-sampled based on IBSI recommendations.[46] Image registration and verification were performed according to a previously published technique.[39] Tumor staging was conducted according to the AJCC 8th edition.[47]

2.2 | Dynamic habitat construction

Figure 1 shows an overview of our methodology, where tumor habitats are identified as unique solutions to the Fokker-Planck equation given pre-treatment and intra-treatment imaging as boundary conditions. Each habitat represents similarity in modeling dynamics for a set of clustered voxels within the tumor. Intra-habitat differences (i.e., 1, 2, 3) represent contrastive dynamics of tumor metabolism during treatment.

2.2.1 | High-dimensional image analysis via Fokker–Planck dynamics

We hypothesized that the time evolution between pre- and intra-treatment PET imaging could be modeled as a continuous process which obeys canonical laws of mathematics. To test this hypothesis, a previously developed method based on Fokker–Planck dynamics[48] was used to construct high dimensional representations of tumors parameterized by PET imaging. In this approach, which is formally known as an equilibrium-driven deformation,[49] ^{18}F-FDG-PET SUV images (pre-treatment and intra-treatment) are interpreted as boundary conditions to solve a mathematical representation of the image evolution. The process is commonly known as "inbetweening auto-animation" and is based on techniques from statistical mechanics. Mathematically, the time evolution of gray-level intensities within an image volume is modeled by the Fokker-Planck equation,[50]

$$\partial_t \rho = \Delta \rho + \nabla \cdot (\rho \nabla \phi) = \nabla \cdot \left(\pi \nabla \left(\frac{\rho}{\pi} \right) \right) \quad (1)$$

where $\rho \in \mathbb{R}^3$ represents the gray-level intensities of the image and $\pi \propto e^{\phi}$ defines the equilibrium density function (i.e., a Gibbs measure[51]) which is a stationary solution to Equation 1. The variable ϕ is the system Hamiltonian, and by analogy to classical mechanics, can be interpreted as the energy of the system. For our application, we interpret this as the potential force which drives evolution between the pre- and intra-treatment images.[38] Specifically, the intra-treatment PET image defined an "energy landscape", that is, the driver of a potential force that uniquely determines the evolution between the initial condition (pre-treatment image) and the equilibrium (intra-treatment image). We argue that this is an appropriate formalism, as the intra-treatment PET image contains extensive information about the disease metabolism in response to (chemo)radiation therapy. Given that the disease phenotype is captured in detail by PET imaging, we argue that the energy landscape derived from the intra-treatment imaging defines a reasonable driving force between the initial (pre-treatment) and equilibrium (intra-treatment) states.

Here, ρ_0, which is defined by the pre-treatment PET image in units of SUV, satisfies the following constraint,

$$\int \rho_0 \, dx = \int \pi \, dx. \quad (2)$$

The pre-treatment and intra-treatment images define no-flux boundary conditions of the Fokker-Planck equation (Equation 1). This is expressed mathematically by the following equation,

$$n \cdot \nabla \left(\frac{\rho}{\pi} \right) = 0 \text{ on } \partial \Omega \quad (3)$$
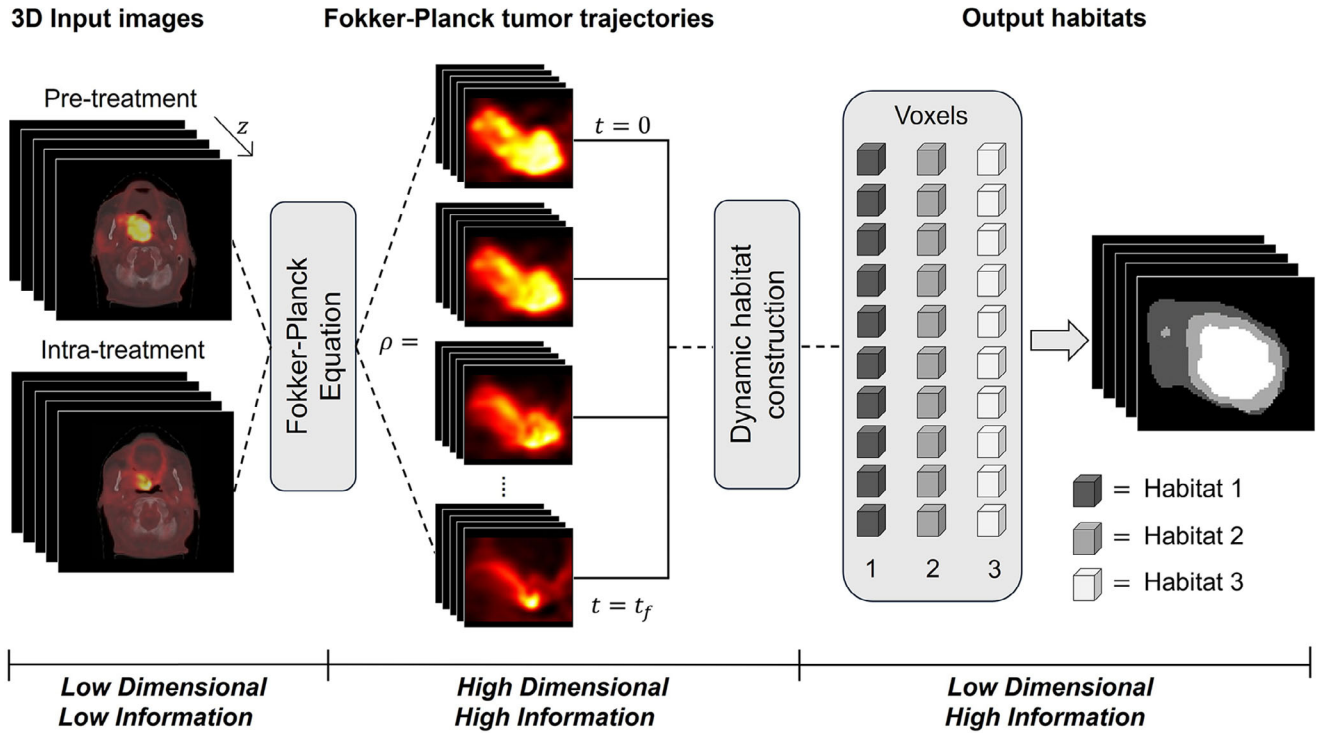
FIGURE 1 Habitat construction methodology. Temporally registered PET images were input into a Fokker-Planck based algorithm which generated mathematical representations of the in-between images. The resulting tensor object was used to identify spatial tumor habitats based on metabolic expression of tumors during treatment.

where, n defines the normal vector to the boundary surface, $\partial\Omega$. Equation 1 was solved numerically using a previously published finite-volume method on structured grids.[52]

The solution of Equation 1 is a 4D tensor (three spatial dimensions and one temporal dimension) that describes the simulated time evolution between the pre- and intra-treatment images. This can be expressed mathematically by the tensor Ψ, where

$$\Psi \subset \mathbb{R}^4 = \left\{ (x, y, z, t) \,|\, x, y, z \in \mathbb{R}, t \in \mathbb{R}^+ \right\} \quad (4)$$

2.2.2 | Spatial habitat construction using a fuzzy clustering algorithm

Equations 1–4 were applied to the PET images of patients on NCT01908504, where Ψ represents the simulated image dynamics of each patient. To identify spatial tumor habitats of Ψ, a fuzzy c-means clustering algorithm was used to partition voxels into separate groups based on local similarity in the time dynamics.[53] First, N tumor voxel indices were extracted by a simple binary search algorithm applied to the gross tumor contour. The corresponding values of ρ were sorted into vectors x_j,

$$\boldsymbol{x}_j = \left[x_{j\,1}, x_{j\,2}, x_{j\,3}, \ldots, x_{j\,T} \right], 1 \leq j \leq N \quad (5)$$

where, T is the number of time points and each vector $\boldsymbol{x}_j$ represents the time evolution of a given tumor voxel. Cluster centers were computed by the algorithm and defined by the vectors $\boldsymbol{c}_i$,

$$\boldsymbol{c}_i = \left[c_{i\,1}, c_{i\,2}, c_{i\,3}, \ldots, c_{i\,T} \right], 1 \leq i \leq C \quad (6)$$

where, C is the number of clusters. The fuzzy clustering algorithm then assigns membership values for each vector that represents the degree to which that vector belongs to each cluster. This was accomplished by minimizing the following objective function,

$$J_m = \sum_{i=1}^{C} \sum_{j=1}^{N} \mu_{ij}^m \left(d_{ij} \right)^2. \quad (7)$$

Here, $m > 1$ is an exponent that controls the *fuzziness* of the clustering algorithm (i.e., the degree of overlap between distinct clusters), μ_{ij}^m is the membership value for the jth vector of the ith cluster (corresponding to a particular exponent m), and d_{ij} is the Euclidean distance from the jth vector to the ith cluster,

$$d_{ij} = \|\boldsymbol{x}_j - \boldsymbol{c}_i\|^2 \quad (8)$$

where, $\|\cdot\|$ is the standard L^2 norm. Cluster centers, membership values, and Euclidean distances

were iteratively computed until the objective function reached a pre-defined minimum threshold value. Each voxel was then assigned to the cluster with maximum membership value. Tumor habitat masks were created by assigning each voxel within the gross tumor the appropriate cluster index.

As the optimal number of clusters to use in fuzzy clustering algorithms is non-trivial, we calculated a validity index[54] and performed fuzzy clustering 10 times, changing the number of clusters from 2 to 11. This procedure was repeated using imaging data from each patient included in the study, which yielded a patient-specific validity index. The optimal number of clusters was defined as the number of clusters which minimized the validity index for each patient. Finally, the overall number of clusters was chosen as the most frequent optimal value across all patients. For our dataset, the optimal number of clusters was determined to be 3.

In addition, the optimal number of timepoints from which to sample the tensor defined by Equation 4 required a quantitative evaluation based on habitat-derived metrics. To address this, we constructed habitats for each patient using multiple values of T (from 1 to 50) and characterized differences in the resulting habitats. To identify the optimal value, we used the ratio of habitat volumes as a stability metric. Specifically, we calculated the habitat volumes for each patient (normalized to tumor volume) and took the mean to obtain an aggregate measure of the habitat volume ratios across the entire patient cohort. This process was repeated for different values of T. We then plotted the mean habitat volume of each habitat against T and then calculated the moving variance to determine the minimum value of T such that the mean volume became stable for each habitat.

To quantify the robustness of our habitat construction algorithm, we used a silhouette metric.[55] The silhouette metric measures both intra-habitat consistency (cohesion) and inter-habitat separability (separation). For a given point i (in this case the value of voxel i), the silhouette metric s is defined as

$$s_i = \frac{b_i - a_i}{\max(a_i, b_i)} \tag{9}$$

where, a_i is the mean distance between i and all other points within the same cluster and b_i represents the minimum mean distance between i and points in a different cluster. For each patient, voxel-specific silhouette metrics were calculated and subsequently averaged to quantify the habitat quality with a single number. These mean silhouette metrics were then plotted across patients and an overall metric, known as the silhouette coefficient, was defined,

$$SC = \max_C \bar{s}(C) \tag{10}$$

where, $\bar{s}$ is the average of silhouette metrics (Equation 9) taken over all patients and C is the number of clusters. The silhouette metric ranges from -1 to 1, with values close to 1 indicating well defined and separated clusters. Silhouette coefficients above 0.7 indicate robust clusters, and silhouette coefficients above 0.5 indicate reasonable clusters.[56] To ensure self-consistency when comparing habitats across patients, we sorted each habitat in decreasing order by volume.

2.3 | Habitat-specific radiomic feature extraction

Radiomic features were extracted to characterize each tumor habitat. Feature extraction was performed using an externally validated,[57] IBSI-benchmarked[46] radiomics platform.[58] Images were discretised using a fixed-bin number (FBN) method with 64 gray levels, justified based on prior work.[59] Habitat specific intensity masks were created through voxel-wise multiplication of each habitat mask (constructed using the method described in Section 2.2.2) and the pre-treatment SUV image. This yielded 3 intensity masks for each patient, from which 54 radiomic texture features were extracted. The list of radiomic features extracted is provided in Table S2. To mitigate potential bias introduced by variation in habitat volume,[60] radiomic features were scaled by a weighting factor W, defined as the normalised habitat volume,

$$W_i = \frac{V_i}{V_{\text{total}}} \tag{11}$$

where, V_i is the volume of the ith tumor habitat for a given patient. The resulting feature space can be mathematically described by the set of matrices

$$\mathcal{F} = \{\mathcal{F}_1, \mathcal{F}_2, \mathcal{F}_3\} \tag{12}$$

where,

$$\mathcal{F}_K = (f_{i,j}) \in \mathbb{R}^{m \times n} \tag{13}$$

is the radiomic feature space corresponding to the Kth habitat ($K = 1, 2, 3$), and the coordinates (i, j) represent the ith radiomic feature observed for the jth patient. Each feature vector was normalized to zero-mean and unit variance. To ensure repeatability of radiomic features extracted, we performed a sensitivity analysis by repeating the habitat construction and feature extraction five times. For comparison, the same radiomic features were extracted from the GTV and the peritumoral region, defined as a 3-mm wide annular region enclosing the GTV.[61]

MEDICAL PHYSICS

TABLE 1 Average morphology features for each habitat across the patient cohort.

Habitat number	Volume [cm^3]	Surface Area [cm^2]	Surface-to-volume ratio	Compactness 1	Sphericity
1	14.56	83.85	6.89	0.012	0.36
2	10.07	59.15	7.20	0.013	0.39
3	5.79	22.81	5.14	0.032	0.70

2.4 | Association of habitat-derived radiomic features with clinical outcomes

We implemented a univariate feature selection process to identify potential drivers of prognostic signal. Kaplan–Meier survival curves were calculated for each feature, where the patient cohort was separated into two groups by the median feature value, and log-rank tests were used to assess statistical significance ($p < 0.05$).[62] Analysis was conducted using the MATLAB-based survival analysis package *MATSURV*.[63]

To calculate the risk score, multivariate Cox proportional hazards models were defined using the features selected above as covariates. Additionally, SUVmax was included as a covariate to test if our method could augment standard image-based intensity metrics. Models were built using the MATLAB function *coxphfit*. We defined the risk score for the jth patient, $RS_j = \sum_{i=1}^{N} f_{ij} b_i$, where f_{ij} is the ith feature value and b_i is the corresponding Cox model coefficient.[64] The risk score was assessed for prognostic value through Kaplan-Meier analysis, where a log-rank p-value less than 0.05 was considered statistically significant.

To demonstrate the potential added utility of our Fokker-Planck algorithm, we compared this risk score with an equivalent derived only from the averaged pre- and intra-treatment images. Furthermore, we compared our radiomic features extracted from the dynamic habitats with benchmark features extracted from the GTV and peritumoral region.

3 | RESULTS

3.1 | Dynamic tumor habitat analysis

3.1.1 | Tumor habitat visualisation

Implementation of the habitat construction methodology outlined in Section 2.2 yielded patient specific dynamic tumor habitats (Figure 2). Tumor habitats varied in phenotype among patients based on differences in image time dynamics according to the Fokker-Planck algorithm. As shown in Figures 2 and 3, tumor habitats qualitatively reflected spatial sub-compartments of disease.

Representative morphology features, averaged across the patient cohort, are shown in Table 1.

3.1.2 | Timepoint sampling frequency

Implementation of the parameter selection process described in Section 2.2.2 yielded an optimal sampling frequency of 18 in-between timepoints. Figures 4 and 5 show the criteria used to select this value, where stability in the variance of habitat volume ratios (Figure 5) was identified as a surrogate for stability in the habitat construction algorithm.

The distributions of habitat volumes for individual patients across timepoint sampling frequencies are shown in Figures S1, S2, and S3.

3.1.3 | Habitat consistency

Quantification of habitat consistency demonstrated the robustness of our methodology (Figure 6). Calculation of silhouette coefficients for each patient (Figure 6a) revealed a minimum value of 0.57 and a maximum value of 0.8. Most patients had silhouette coefficients between 0.5 and 0.7, which indicated reasonable intra-habitat consistency. Furthermore, 14 patients had silhouette coefficients above 0.7, suggesting robust tumor habitats. Figure 6b shows illustrating examples of silhouette plots for two patients: one with the lowest intra-habitat consistency, that is, the least robust habitats; and one with the highest intra-habitat consistency, that is, the most robust habitats. The silhouette plot groups all voxels within a given habitat and plots the corresponding silhouette metrics (Equation 9). The ideal case would be all points equal to 1 for each habitat, that is, the plot would appear rectangular with each horizontal line having a length of one. The degree to which each group "falls off" indicates the amount of inconsistency in each habitat. Voxels with negative silhouette metrics are the least consistent with the rest of the voxels within a habitat.

3.2 | Prognostic value of habitat-derived radiomics

Univariate feature selection performed using Kaplan–Meier survival curves and log-rank tests revealed
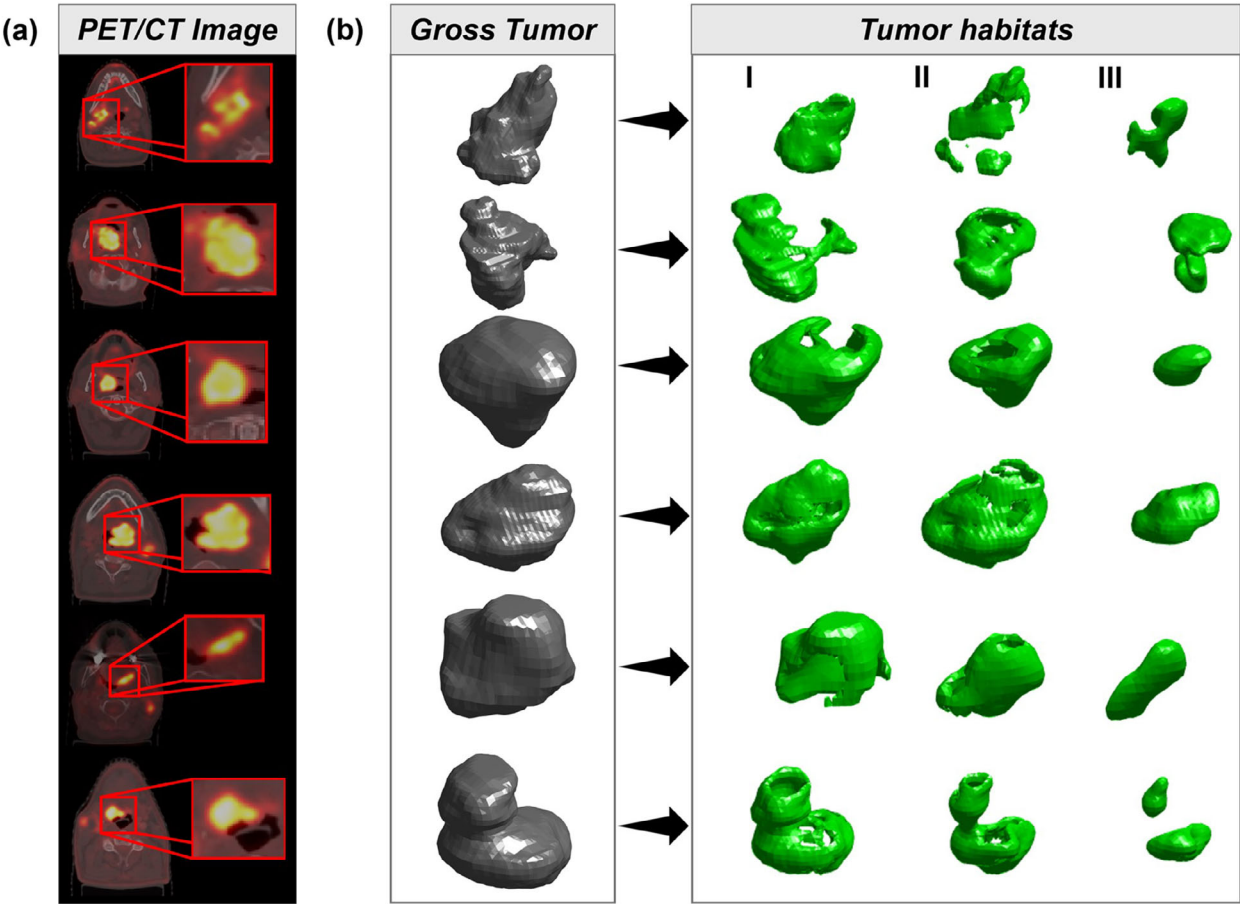
FIGURE 2 Visualisation of tumor habitats for six representative patients. (a) Axial slices of PET/CT images illustrating metabolic activity of OPC tumors. (b) Volumetric renderings of the gross tumor volume and the dynamic tumor habitats generated in our study, in decreasing order of habitat volume.

TABLE 2 Statistical results from feature selection and Cox proportional hazards model.

Habitat Number	Feature family	Feature Name	Log-rank p-value	Hazard Ratio (95% CI)	Cox Regression coefficient
3	GLRLM	Normalized run-length non-uniformity	0.0073	4.67 (1.75–12.5)	−0.0397
3	GLRLM	Run percentage	0.0085	4.55 (1.71–12.1)	1.0590
3	GLRLM	Short run emphasis	0.0396	3.05 (1.14–8.12)	−0.6700
3	GLCOM	Sum entropy	0.0396	3.05 (1.14–8.12)	−0.7774
3	GLCOM	Joint entropy	0.0396	3.05 (1.14–8.12)	0.7245
3	GLSZM	Zone size entropy	0.0048	4.97 (1.86–13.3)	−0.3984
3	GLSZM	Large Zone Emphasis	0.0238	3.36 (1.26–8.97)	−7.4720
3	GLSZM	Zone size variance	0.0238	3.36 (1.26–8.97)	7.1658
N/A	N/A	SUVmax	0.045	2.97 (1.11–7.91)	−0.8502

habitat-specific radiomic features that were associated with recurrence free survival. These statistical parameters and multivariate Cox regression coefficients are summarized in Table 2. Notably, all prognostic features were derived from habitat 3 and included

three run-length matrix features,[65] two co-occurrence matrix features,[66] and three size-zone matrix features.[67]

Potential confounding surrogates for these features, that is, mean SUV, and tumor volume, were tested for sta-
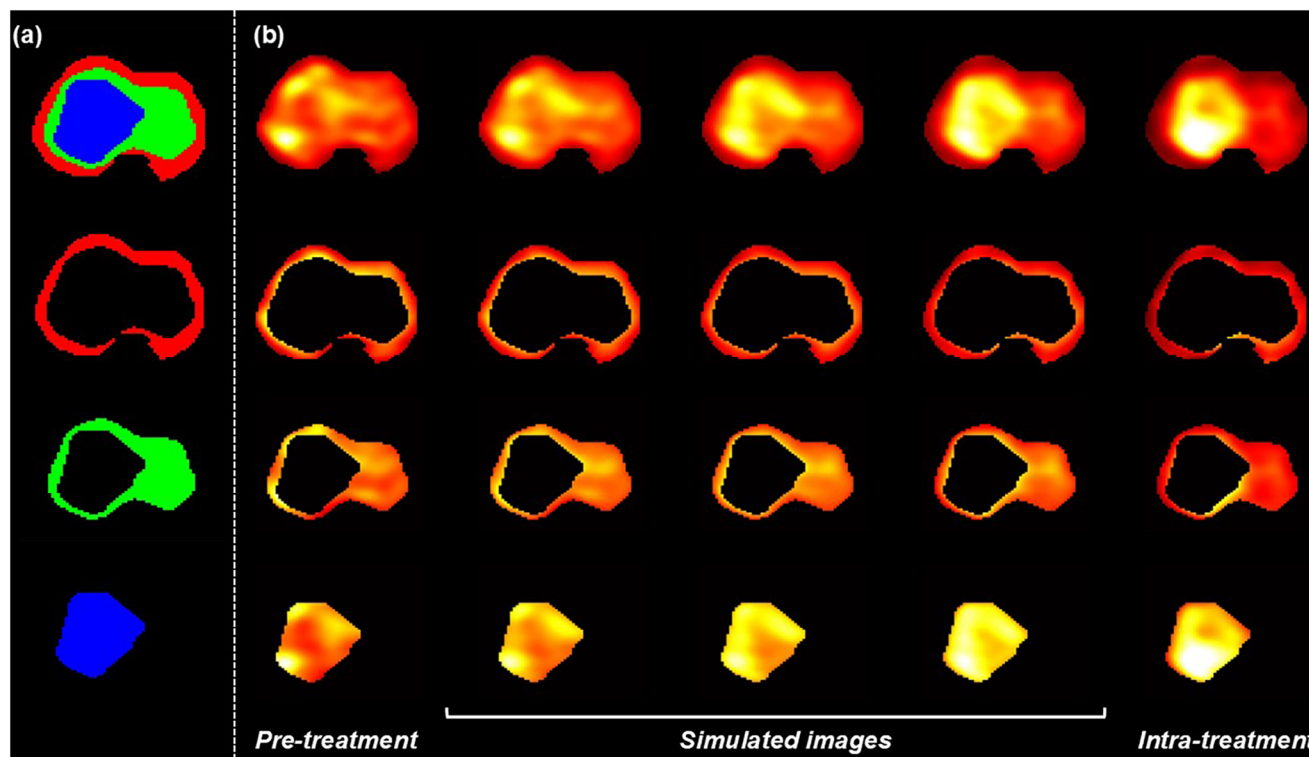
FIGURE 3 (a) Axial visualisation of habitat masks for a representative patient. (b) Image evolution according to the Fokker-Planck equation, separated by tumor habitat, which highlights the heterogenous tumor metabolism throughout the treatment period.
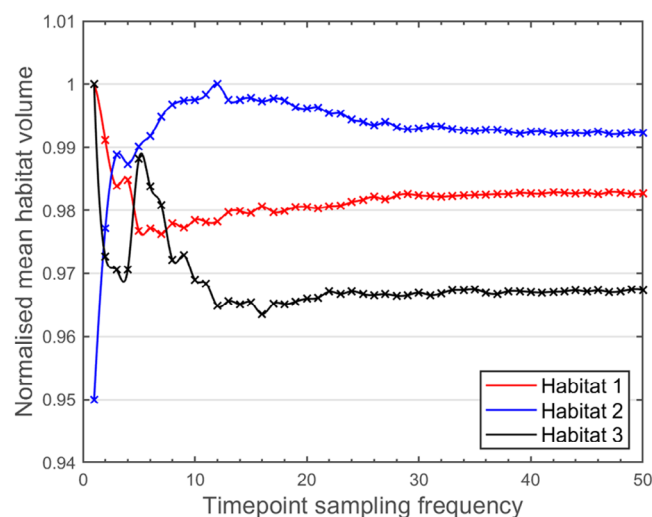

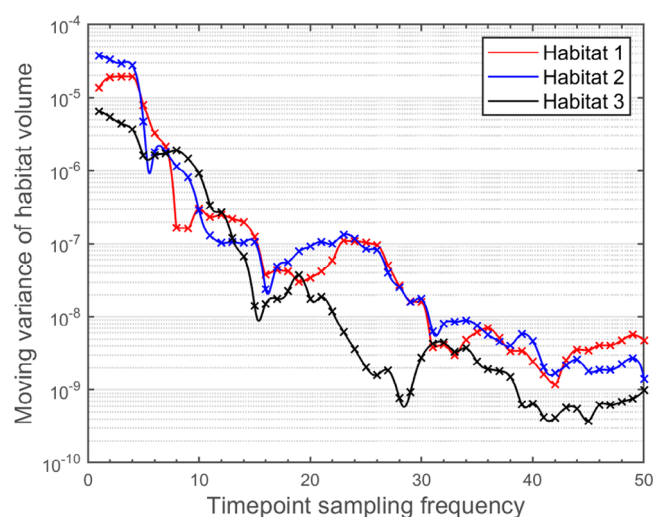**FIGURE 4** Change in mean habitat volume as sampling frequency is increased.

FIGURE 5 Variance in habitat volume calculated using a sliding window to visualise the stability of the algorithm as the timepoint sampling frequency is increased.

tistical significance and were not prognostic ($p = 0.430$ and $p = 0.110$, respectively). SUVmax was found to be associated with recurrence-free survival ($p = 0.045$), indicating a potential advantage over other common aggregate metrics (Figure 7b). Our radiomic sensitivity analysis revealed no variation in features extracted when the process was independently repeated five times.

Calculation of the patient specific risk score and stratification of the patient cohort by median risk score value allowed for the construction of a Kaplan-Meier survival curve (Figure 7a). This survival curve demonstrated statistically significant ($p = 0.032$) separation of patients by median risk score. The equivalent risk score derived from only the pre- and intra-treatment images (i.e., without using the Fokker–Planck algorithm to generate
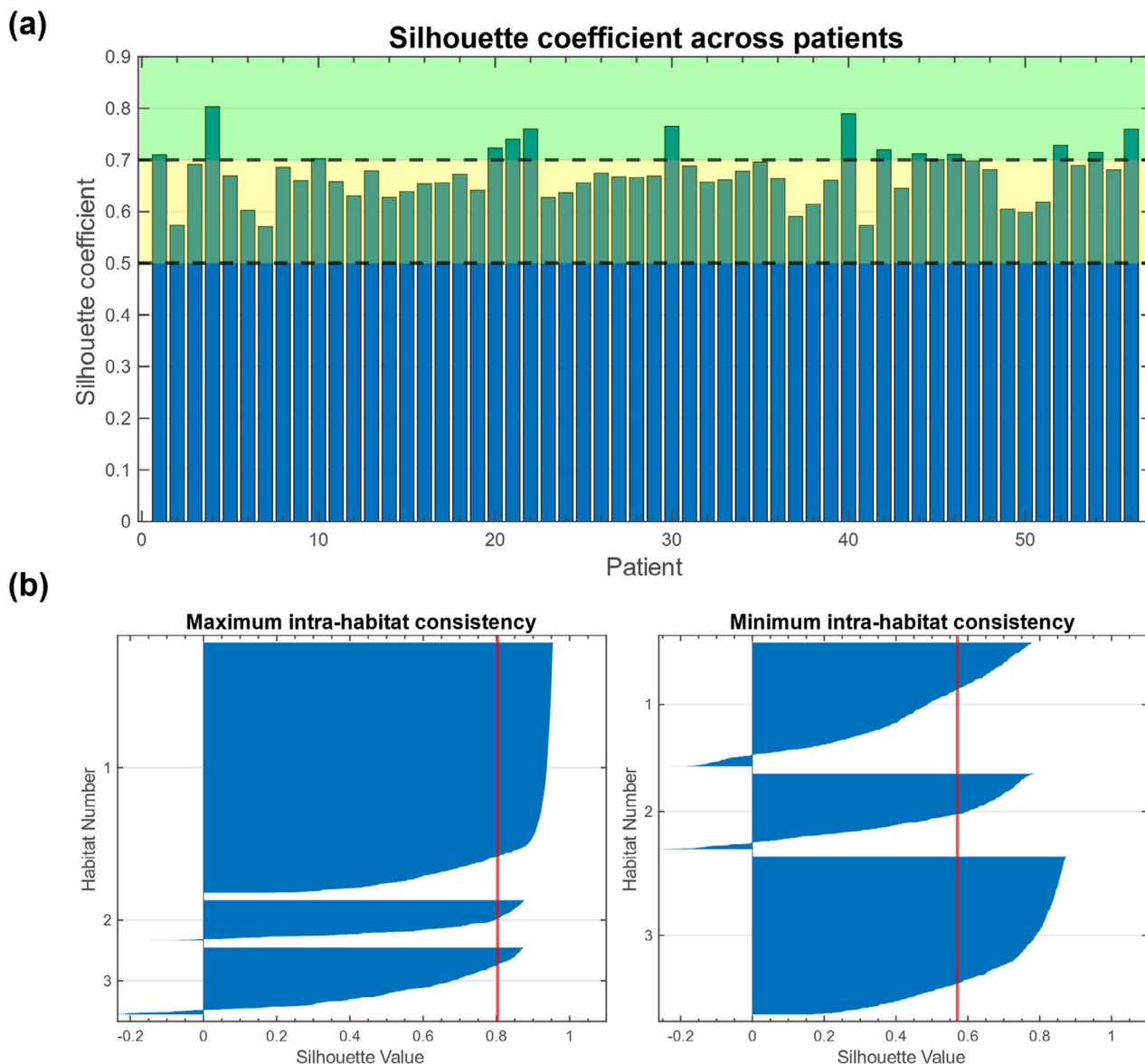
(a)

(b)

FIGURE 6 Quantifying habitat quality. (a) Silhouette coefficient (Equation 10) for each patient in the study. The green region represents patients with very consistent tumor habitats, and the yellow region represents patients with consistent tumor habitats. (b) Representative silhouette plots for the patients with the most (SC = 0.8) and least (SC = 0.57) robust tumor habitats. Silhouette coefficients, that is, the mean of all silhouette metrics for a given patient, are indicated by the vertical red lines.

approximate image dynamics) was not associated with recurrence-free survival ($p = 0.102$). Additionally, benchmark features extracted from the GTV and peritumoral region did not yield a prognostic risk score (for further details, see Figures S6, S7, and S8). This highlights the importance of the dynamical aspect of our work.

4 | DISCUSSION

In this study, we designed a novel algorithm to construct dynamic tumor habitats based on the application of mathematical models and demonstrated an application

of our technique to oropharyngeal cancer. The key innovation in our work is the method of habitat construction based on modeling image dynamics during therapy. Other studies have argued for the importance of habitats to study spatial heterogeneity in oropharyngeal tumors. However, the majority are based on image thresholding approaches, for example, the Otsu method which maximises the variance between groups of voxels to construct habitats. While these approaches can provide useful information, they can only capture spatial heterogeneity at a particular snapshot in time. Our approach incorporates dynamics directly into habitat construction. The field of study from which the
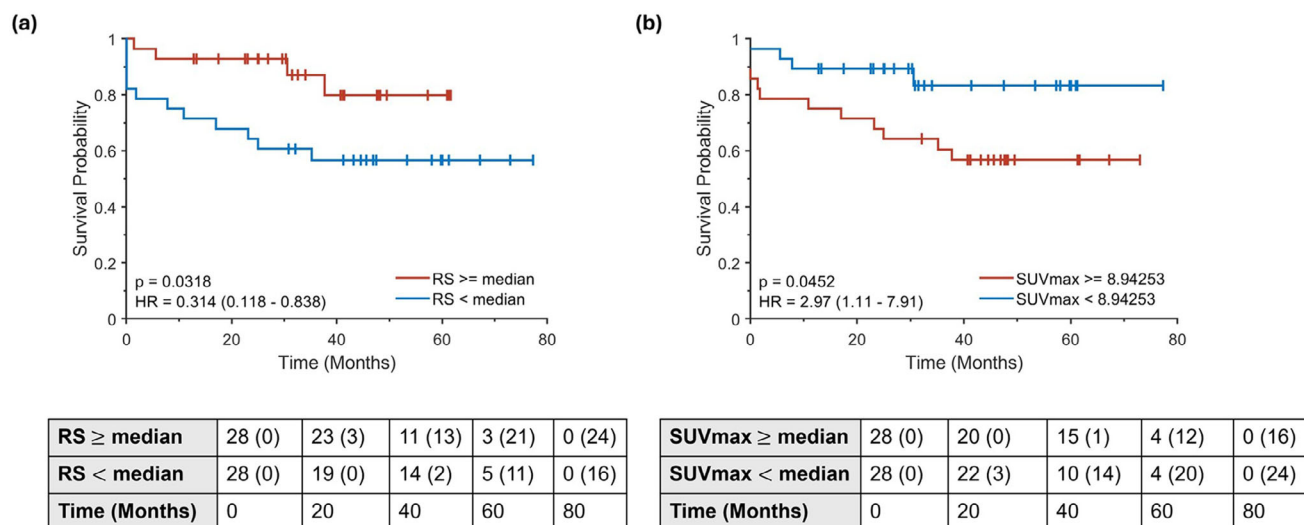
FIGURE 7 Prognostic value of the habitat-derived risk score. (a) Kaplan–Meier curve and risk table demonstrating statistically significant separation of the patient group by median risk score value. (b) Kaplan–Meier curve and risk table where patients are stratified by median SUV-max, which highlights the potential prognostic benefit of this metric.

mathematical model originates, that is, statistical mechanics, focuses on the characterisation of complex physical systems by their macroscopic behavior. While studying each microscopic component of a system may provide a complete description of its physical behavior, this quickly becomes intractable when applied to real life problems. The innovation of our work is the application of these traditional physics techniques to solve problems in medicine, realising that the fundamental methods are independent of the specific application. Our results demonstrate new radiomics data that is more specific to different compartments of the disease and based on differences in local tumor response during treatment.

Our dynamic tumor habitat analyses revealed spatial heterogeneity in the evolution of metabolic activity measured on SUV images of patients with OPC. This heterogeneity was characterized using habitat-specific radiomics features, which were then used to construct a prognostic risk score. We showed that separating tumors into sub-regions based on metabolic activity over time can provide useful information when combined with high throughput radiomics techniques. There are a several potential explanations for the prognostic signal that we observed. By separating the gross tumor into spatial subregions, we increased the amount of information that can be used in downstream radiomics analysis. Our habitats may therefore describe the gross disease in finer detail than previously studied methods, such as regions of aerobic disease and/or regions of hypoxic disease.[14,19,68] Furthermore, given that the mathematical model was defined using both pre- and intra-treatment imaging, dynamic habitats may also reveal information about differential resistance to radi-

ation therapy. Future work will aim to translate the habitats constructed in this study to potential biological phenomena (e.g., hypoxia, immune dysregulation, etc.).

Qualitatively, we observed similar patterns in habitat formation across most of the patient cohort. In 55 of the 56 patients studied, habitat 3 (i.e., the smallest by volume) corresponded to an interior region of the GTV which could represent the tumor core. Furthermore, 46 patients had habitats that were consistent with those shown in Figure 3, that is, the largest habitat corresponded to the tumor periphery. These observations are particularly intriguing, given that our algorithm was based on an unsupervised clustering approach. Therefore, we hypothesize that there exist some intrinsic similarities between these distinct regions that was captured by our dynamic algorithm. However, as this study was data-driven and conducted with a relatively small sample size, we cannot make broader interpretations of these results. Future work on independent, prospective trial data could confirm the preliminary findings presented in this study.

Some studies have suggested that the central tumor region corresponds to the highest metabolic uptake,[69] and others have linked regions of greater metabolism with higher radioresistance.[70,71] Therefore, it is possible that the innermost habitat represents the most aggressive and nonresponsive area of the disease and drives patient outcomes. While these interpretations are currently speculative, characterization of the tumor microenvironment and linking it to patient outcomes is an exciting research frontier.

Numerous prior studies have argued the importance of spatial heterogeneity in the characterization of underlying tumor phenotype across various imaging

modalities and disease sites. MRI is often used to define spatial tumor habitats due to the large amount of anatomical/physiological information that can be captured. Bailo, et al.[12] investigated spatial heterogeneity, hypoxia, and perfusion in malignant gliomas utilizing diffusion-weighted MRI and PET imaging. Similarly, Jeong, et al.[41] investigated the physiology of CNS lymphoma by constructing tumor habitats based on ADC and cerebral blood volume measurements from susceptibility MR imaging. Quantitative MR habitat analyses have also been used to assess treatment response in the tumor microenvironment for breast cancer patients[42,45] and to differentiate radionecrosis from disease recurrence.[43,44] Beyond MR, habitat derived PET/CT radiomics has shown promise in predicting mutation of colorectal cancer[16] and survival of patients with high-grade ovarian cancer.[15] Our work complements these studies and is especially unique due to the longitudinal nature of our data, as we can extend our analyses to the dynamics of the tumor microenvironment.

Prior work has already identified that intratumor heterogeneity can pose a challenge for personalized medicine. Specifically, genomic and molecular biopsy-based assays often represent only small sub-regions of the tumor, as opposed to the entire phenotype.[72,73] This is further complicated when radiation, which represents a significant perturbation of the underlying biology, is introduced. Indeed, differential rates of cell killing in various subclonal regions of the gross disease could be a contributing factor in the tumor habitats that were observed in this study. Spatial variation in radiosensitivity, which is potentially captured by our tumor habitats, could represent an important aspect of response to radiation therapy. Further work, including incorporation of radiation-induced cell killing, such as the lethal and potentially lethal (LPL) model,[74] may lead to additional insight on the relationship between spatial tumor habitats and radiation therapy.

In this work, we did not directly encode the effects of radiation dose into our algorithm. Since the dataset that we used was from a prospective trial with a uniform dose prescription regime, we argue that direct modelling of radiation dose was not necessary in this preliminary study. Furthermore, other studies using the same dataset have shown that dosimetry is a shallow feature, and that the most important information can be derived from the PET signal alone.[36] However, incorporating dose information into our algorithm is a natural extension and prior studies have already shown promising results when incorporating radiation dose into deterministic models, specifically when integrating the result into deep learning frameworks.[39] In the future, we aim to combine models of radiation dose with patient specific dose distributions to capture heterogeneities that are induced by treatment. Furthermore, we did not include low dimensional clin-ical features in the multivariate Cox model in this work. These features were not associated with recurrence free survival when tested using univariate or multivariate analyses. However, emerging data-fusion methodologies[75] that can integrate low dimensional clinical features with high dimensional radiomics features may enhance the clinical interpretability of future studies.

Our work presents an original method for constructing dynamic tumor habitats, but there are some key limitations that warrant discussion. The main limitation of this study is the lack of an independent dataset for external validation. Our analysis is based on data from a recently completed prospective clinical trial, where intra-treatment PET images were acquired via a standardized, prospectively controlled imaging protocol on a single scanner. This limits immediate external validation, and so the current TRIPOD[76] Type 1a study was conducted to demonstrate apparent performance and produce hypothesis generating data. That said, the core impact of this work lies not in the specific clinical findings, but in the development of a generalized algorithmic framework and the introduction of dynamic habitats as a model for spatiotemporal tumor heterogeneity. While c-means clustering involves tuneable parameters that should eventually be evaluated on external data, the solutions to the Fokker–Planck equation are deterministic and patient-specific. Model parameters are therefore not learned from population data, but rather fit individually for each patient, reducing the risk of overfitting and enhancing interpretability. Nevertheless, external validation remains an important future step to maximize scientific value.

Furthermore, our feature selection algorithm used to identify potential drivers of prognostic signal was rudimentary. Given the number of features extracted was much greater than the sample size, a feature selection algorithm was required. Univariate feature selection methods are not unprecedented,[77] but there are many other possible feature selection algorithms to choose from,[78] which often rely on splitting the data into separate training and testing sets. However, recent work[79] has shown that in the case of small datasets, the particular split into training and testing sets can change the resulting analysis. Given the size of our dataset, we chose a simple univariate feature selection algorithm to avoid these types of issues. In the future, we plan to address this limitation by using a larger dataset and investigating different feature selection algorithms to enhance the robustness of our findings. Larger sample sizes may also allow for more advanced feature selection methods that have already shown promise in radiomics studies, such as principal component analysis (PCA).[80] We confirmed that the prognostic signal observed in Figure 7 was reflected qualitatively when the sampling frequency was changed (see Figures S4 and S5 for examples).

5 | CONCLUSION

Qualitative differences in habitat morphology suggested connections between habitats and response to therapy, such as tumor shrinkage. Key parameters, such as timepoint sampling frequency and optimal number of clusters were quantitatively derived from the patient dataset. The derived patient-specific risk score demonstrated prominent patient outcome prognostic value in multivariate analysis. Our study provides a preliminary approach to a more nuanced understanding of tumor heterogeneity, with potential implications for patient-specific precision oncology.

DATA AVAILABILITY STATEMENT
Research data are stored in an institutional repository, and deidentified data will be shared upon request to the corresponding author through a data use agreement.

REFERENCES

1. Siegel RL, Miller KD, Wagle NS, Jemal A. Cancer statistics. *CA Cancer J Clin*. 2023;73(1):17-48. doi:10.3322/caac.21763

2. Bentzen SM, Trotti A. Evaluation of early and late toxicities in chemoradiation trials. *J Clin Oncol*. 2007;25(26):4096-4103. doi:10.1200/JCO.2007.13.3983

3. Adelstein DJ, Ismaila N, Ku JA, et al. Role of treatment deintensification in the management of p16+ oropharyngeal cancer: aSCO provisional clinical opinion. *J Clin Oncol*. 2019;37(18):1578-1589. doi:10.1200/JCO.19.00441

4. Chaturvedi AK, Engels EA, Pfeiffer RM, et al. Human papillomavirus and rising oropharyngeal cancer incidence in the United States. *J Clin Oncol*. 2011;29(32):4294-4301. doi:10.1200/JCO.2011.36.4596

5. O'Sullivan B, Huang SH, Su J, et al. Development and validation of a staging system for HPV-related oropharyngeal cancer by the International Collaboration on Oropharyngeal Cancer Network for Staging (ICON-S): a multicentre cohort study. *Lancet Oncol*. 2016;17(4):440-451. doi:10.1016/S1470-2045(15)00560-4

6. Ang KK, H J, Wheeler R, et al. Human papillomavirus and survival of patients with oropharyngeal cancer. *N Engl J Med*. 2010;363(1):24-35. doi:10.1056/NEJMoa0912217

7. Brizel DM. Head and neck cancer as a model for advances in imaging prognosis, early assessment, and posttherapy evaluation. *Cancer J*. 2011;17(3):159-165. doi:10.1097/PPO.0b013e31821e8a09

8. Goel R, Moore W, Sumer B, Khan S, Sher D, Subramaniam RM. Clinical practice in PET/CT for the management of head and neck squamous cell cancer. *AJR Am J Roentgenol*. 2017;209(2):289-303. doi:10.2214/AJR.17.18301

9. Sjovall J, Chua B, Pryor D, et al. Long-term results of positron emission tomography-directed management of the neck in node-positive head and neck cancer after organ preservation therapy. *Oral Oncol*. 2015;51(3):260-266. doi:10.1016/j.oraloncology.2014.12.009

10. Lafata KJ, Chang Y, Wang C, et al. Intrinsic radiomic expression patterns after 20 Gy demonstrate early metabolic response of oropharyngeal cancers. *Med Phys*. 2021;48(7):3767-3777. doi:10.1002/mp.14926

11. Mowery YM, Vergalasova I, Rushing CN, et al. Early (18)F-FDG-PET response during radiation therapy for HPV-related oropharyngeal cancer may predict disease recurrence. *Int J Radiat Oncol Biol Phys*. 2020;108(4):969-976. doi:10.1016/j.ijrobp.2020.08.029

12. Bailo M, Pecco N, Callea M, et al. Decoding the heterogeneity of malignant gliomas by PET and MRI for spatial habitat analysis of hypoxia, perfusion, and diffusion imaging: a preliminary study. *Front Neurosci*. 2022;16:885291. doi:10.3389/fnins.2022.885291

13. O'Connor JP, Rose CJ, Waterton JC, Carano RA, Parker GJ, Jackson A. Imaging intratumor heterogeneity: role in therapy response, resistance, and clinical outcome. *Clin Cancer Res*. 2015;21(2):249-257. doi:10.1158/1078-0432.CCR-14-0990

14. Orlhac F, Soussan M, Maisonobe JA, Garcia CA, Vanderlinden B, Buvat I. Tumor texture analysis in 18F-FDG PET: relationships between texture parameters, histogram indices, standardized uptake values, metabolic volumes, and total lesion glycolysis. *J Nucl Med*. 2014;55(3):414-422. doi:10.2967/jnumed.113.129858

15. Wang X, Xu C, Grzegorzek M, Sun H. Habitat radiomics analysis of pet/ct imaging in high-grade serous ovarian cancer: application to Ki-67 status and progression-free survival. *Front Physiol*. 2022;13:948767. doi:10.3389/fphys.2022.948767

16. Zhao H, Su Y, Wang Y, et al. Using tumor habitat-derived radiomic analysis during pretreatment (18)F-FDG PET for predicting KRAS/NRAS/BRAF mutations in colorectal cancer. *Cancer Imaging*. 2024;24(1):26. doi:10.1186/s40644-024-00670-2

17. Brizel DM, Sibley GS, Prosnitz LR, Scher RL, Dewhirst MW. Tumor hypoxia adversely affects the prognosis of carcinoma of the head and neck. *Int J Radiat Oncol Biol Phys*. 1997;38(2):285-289. doi:10.1016/s0360-3016(97)00101-6

18. Kroenke M, Hirata K, Gafita A, et al. Voxel based comparison and texture analysis of 18F-FDG and 18F-FMISO PET of patients with head-and-neck cancer. *PLoS One*. 2019;14(2):e0213111. doi:10.1371/journal.pone.0213111

19. Yamada T, Uchida M, Kwang-Lee K, et al. Correlation of metabolism/hypoxia markers and fluorodeoxyglucose uptake in oral squamous cell carcinomas. *Oral Surg Oral Med Oral Pathol Oral Radiol*. 2012;113(4):464-471. doi:10.1016/j.tripleo.2011.04.006

20. Halfpenny W, Hain SF, Biassoni L, Maisey MN, Sherman JA, McGurk MF. A possible prognostic factor in head and neck cancer. *Br J Cancer*. 2002;86(4):512-516. doi:10.1038/sj.bjc.6600114

21. Machtay M, Natwa M, Andrel J, et al. Pretreatment FDG-PET standardized uptake value as a prognostic factor for outcome in head and neck cancer. *Head Neck*. 2009;31(2):195-201. doi:10.1002/hed.20942

22. Allal AS, Dulguerov P, Allaoua M, et al. Standardized uptake value of 2-[(18)F] fluoro-2-deoxy-D-glucose in predicting outcome in head and neck carcinomas treated by radiotherapy with or without chemotherapy. *J Clin Oncol*. 2002;20(5):1398-1404. doi:10.1200/JCO.2002.20.5.1398

23. Brun E, Kjellén E, Tennvall J, et al. FDG PET studies during treatment: prediction of therapy outcome in head and neck squamous cell carcinoma. *Head Neck*. 2002;24(2):127-135. doi:10.1002/hed.10037

24. Malone JP, Gerberi MAT, Vasireddy S, et al. Early prediction of response to chemoradiotherapy for head and neck cancer: reliability of restaging with combined positron emission tomography and computed tomography. *Arch Otolaryngol Head Neck Surg*. 2009;135(11):1119-1125. doi:10.1001/archoto.2009.152

25. Krabbe CA, Pruim J, Dijkstra PU, et al. 18F-FDG PET as a routine posttreatment surveillance tool in oral and oropharyngeal squamous cell carcinoma: a prospective study. *J Nucl Med*. 2009;50(12):1940-1947. doi:10.2967/jnumed.109.065300

26. Zhong J, Sundersingh M, Dyker K, et al. Post-treatment FDG PET-CT in head and neck carcinoma: comparative analysis of

4 qualitative interpretative criteria in a large patient cohort. *Sci Rep-Uk*. 2020;10(1). doi:10.1038/s41598-020-60739-3

27. Greven, KM. Serial positron emission tomography scans following radiation therapy of patients with head and neck cancer. *Head Neck*. 2001;23(11):942-946. doi:10.1002/hed.1136

28. Vernon MR, Maheshwari M, Schultz CJ, et al. Clinical outcomes of patients receiving integrated PET/CT-guided radiotherapy for head and neck carcinoma. *Int J Radiat Oncol Biol Phys*. 2008;70(3):678-684. doi:10.1016/j.ijrobp.2007.10.044

29. Aerts HJWL, Velazquez ER, Leijenaar RTH, et al. Decoding tumour phenotype by noninvasive imaging using a quantitative radiomics approach. *Nat Commun*. 2014;5:4006. doi:10.1038/ncomms5006

30. Ferris RL, Blumenschein G, Fayette J, et al. Nivolumab for recurrent squamous-cell carcinoma of the head and neck. *N Engl J Med*. 2016(19):1856-1867. doi:10.1056/NEJMoa1602252

31. Pota M, Scalco E, Sanguineti G, et al. Early prediction of radiotherapy-induced parotid shrinkage and toxicity based on CT radiomics and fuzzy classification. *Artif Intell Med*. 2017;81:41-53. doi:10.1016/j.artmed.2017.03.004

32. Bogowicz M, Leijenaar RTH, Tanadini-Lang S. Post-radiochemotherapy PET radiomics in head and neck cancer—The influence of radiomics implementation on the reproducibility of local control tumor models. *Radiother Oncol*. 2017;125(3):385-391. doi:10.1016/j.radonc.2017.10.023

33. Folkert MR, Setton J, Apte AP. Predictive modeling of outcomes following definitive chemoradiotherapy for oropharyngeal cancer based on FDG-PET image characteristics. *Phys Med Biol*. 2017;62(13):5327-5343. doi:10.1088/1361-6560/aa73cc

34. Vallières M, Kay-Rivest E, Perrin LJ. Radiomics strategies for risk assessment of tumour failure in head-and-neck cancer. *Sci Rep*. 2017;7(1):10117. doi:10.1038/s41598-017-10371-5

35. Ger RB, Zhou S, Elgohari B, et al. Radiomics features of the primary tumor fail to improve prediction of overall survival in large cohorts of CT- and PET-imaged head and neck cancer patients. *PLoS One*. 2019;14(9):e0222509. doi:10.1371/journal.pone.0222509

36. Ji H, Lafata K, Mowery Y, et al. Post-Radiotherapy PET image outcome prediction by deep learning under biological model guidance: a feasibility study of oropharyngeal cancer application. *Front Oncol*. 2022;12:895544. doi:10.3389/fonc.2022.895544

37. Lafata K, Zhou Z, Liu J, Yin F. Data clustering based on Langevin annealing with a self-consistent potential. *Quart Appl Math*. 2019;77:591-613. doi:10.1090/qam/1521

38. Stevens JB, Riley BA, Je J, et al. Radiomics on spatial-temporal manifolds via Fokker-Planck dynamics. *Med Phys*. 2024;51(5):3334-3347. doi:10.1002/mp.16905

39. Wang C, Liu C, Chang Y. Dose-distribution-driven pet image-based outcome prediction (DDD-PIOP): a deep learning study for oropharyngeal cancer IMRT application. *Front Oncol*. 2020;10:1592. doi:10.3389/fonc.2020.01592

40. Cherezov D, Goldgof D, Hall L, et al. Revealing tumor habitats from texture heterogeneity analysis for classification of lung cancer malignancy and aggressiveness. *Sci Rep*. 2019;9:4500. doi:10.1038/s41598-019-38831-0

41. Jeong SY, Park JE, Kim N, Kim HS. Hypovascular cellular tumor in primary central nervous system lymphoma is associated with treatment resistance: tumor habitat analysis using physiologic MRI. *Am J Neuroradiol*. 2022;43(1):40-47. doi:10.3174/ajnr.A7351

42. Kazerouni AS, Hormuth DA, Davis T, et al. Quantifying tumor heterogeneity via MRI habitats to characterize microenvironmental alterations in HER2+ breast cancer. *Cancers (Basel)*. 2022;14(7). doi:10.3390/cancers14071837

43. Lee DH, Park JE, Kim HS. Tumor habitat analysis by magnetic resonance imaging distinguishes tumor progression from radiation necrosis in brain metastases after stereotactic radiosurgery. *Neuro-Oncology*. 2021;23:127-127.

44. Lee DH, Park JE, Kim N, et al. Tumor habitat analysis using longitudinal physiological MRI to predict tumor recurrence after stereotactic radiosurgery for brain metastasis. *Korean J Radiol*. 2023;24(3):235-246. doi:10.3348/kjr.2022.0492

45. Syed AK, Whisenant JG, Barnes SL, Sorace AG, Yankeelov TE. Multiparametric analysis of longitudinal quantitative MRI data to identify distinct tumor habitats in preclinical models of breast cancer. *Cancers*. 2020;12(6). doi:10.3390/cancers12061682

46. Zwanenburg A, Vallières M, Abdalah MA, et al. The image biomarker standardization initiative: standardized quantitative radiomics for high-throughput image-based phenotyping. *Radiology*. 2020;295(2):328-338. doi:10.1148/radiol.2020191145

47. Amin MB, Greene FL, Edge SB, et al. The eighth edition AJCC Cancer staging manual: continuing to build a bridge from a population-based to a more "personalized" approach to cancer staging. *CA Cancer J Clin*. 2017;67(2):93-99. doi:10.3322/caac.21388

48. Stevens JB, Riley BA, Je J, et al. Radiomics on spatial-temporal manifolds via Fokker-Planck dynamics. *Med Phys*. 2024. doi:10.1002/mp.16905

49. Gao Y, Liu JG, Wu N. Data-driven efficient solvers for Langevin dynamics on manifold in high dimensions. *Appl Comput Harmon A*. 2023;62:261-309. doi:10.1016/j.acha.2022.09.003

50. Medved A, Davis R, Vasquez PA. Understanding fluid dynamics from Langevin and Fokker-Planck equations *Fluids*. 2020;5(1):40. doi:10.3390/fluids5010040

51. Georgii H-O. *Gibbs Measures and Phase Transitions. De Gruyter Studies in Mathematics*. W de Gruyter; 1988:525.

52. Gao Y, Jin GZ, Liu JG. Inbetweening auto-animation via fokker-planck dynamics and thresholding. *Inverse Probl Imag*. 2021;15(5):843-864. doi:10.3934/ipi.2021016

53. Bezdek JC. *Pattern Recognition with Fuzzy Objective Function Algorithms*. Plenum Press; 1981:256.

54. Xie XL, Beni G. A validity measure for fuzzy clustering. *IEEE Transactions on Pattern Analysis and Machine Intelligence*. 1991;13(8):841-847. doi:10.1109/34.85677

55. Rousseeuw PJ. Silhouettes: a graphical aid to the interpretation and validation of cluster analysis. *J Comput Appl Math*. 1987;20:53-65. doi:10.1016/0377-0427(87)90125-7

56. Kaufman L, Rousseeuw PJ. *ProQuest. Finding Groups in Data: An Introduction to Cluster Analysis*. Wiley; 1990.

57. Chang Y, Lafata K, Wang C, et al. Digital phantoms for characterizing inconsistencies among radiomics extraction toolboxes. *Biomed Phys Eng Express*. 2020;6(2):025016. doi:10.1088/2057-1976/ab779c

58. Lafata KJ, Novel identification of radiomic biomarkers with Langevin annealing. Duke University; 2018.

59. Riley BA, Stevens JB, Li X, et al. Prognostic value of different discretization parameters in (18)fluorodeoxyglucose positron emission tomography radiomics of oropharyngeal squamous cell carcinoma. *J Med Imaging*. 2024;11(2):024007. doi:10.1117/1.JMI.11.2.024007

60. Roy S, Whitehead TD, Quirk JD, et al. Optimal co-clinical radiomics: sensitivity of radiomic features to tumour volume, image noise and resolution in co-clinical T1-weighted and T2-weighted magnetic resonance imaging. *EBioMedicine*. 2020;59:102963. doi:10.1016/j.ebiom.2020.102963

61. Lin P, Xie W, Li Y, et al. Intratumoral and peritumoral radiomics of MRIs predicts pathologic complete response to neoadjuvant chemoimmunotherapy in patients with head and neck squamous cell carcinoma. *J Immunother Cancer*. 2024;12(11). doi:10.1136/jitc-2024-009616

62. Clark TG, Bradburn MJ, Love SB, Altman DG. Survival analysis part I: basic concepts and first analyses. *Br J Cancer*. 2003;89(2):232-238. doi:10.1038/sj.bjc.6601118

63. Creed J, Gerke T, Berglund A. MatSurv: survival analysis and visualization in MATLAB. *J Open Source Software*. 2020;5:1830.

64. Xu T, Yuan Y, He C, Yang K. Construction and evaluation of a risk score model for autophagy-related genes in esophageal adenocarcinoma. *Med Sci Monit*. 2021;27:e927850. doi:10.12659/MSM.927850

65. Galloway MM. Texture analysis using gray level run lengths. *Comput Graph Image Process*. 1975;4(2):172-179. doi:10.1016/S0146-664X(75)80008-6

66. Haralick RM, Shanmugam K, Dinstein I. Textural features for image classification. *IEEE Trans Sys Man Cybern*. 1973;3(6):610-621. doi:10.1109/TSMC.1973.4309314

67. Thibault G, Angulo J, Meyer F. Advanced statistical matrices for texture characterization: application to cell classification. *IEEE Trans Bio-Med Eng*. 2014;61(3):630-637. doi:10.1109/TBME.2013.2284600

68. Thorwarth D, Eschmann SM, Holzner F, Paulsen F, Alber M. Combined uptake of [18F]FDG and [18F]FMISO correlates with radiation therapy outcome in head-and-neck cancer patients. *Radiother Oncol*. 2006;80(2):151-156. doi:10.1016/j.radonc.2006.07.033

69. Bosque JJ, Calvo GF, Molina-García D, Pérez-Beteta J, García Vicente AM, Pérez-García VM. Metabolic activity grows in human cancers pushed by phenotypic variability. *iScience*. 2023;26(3):106118. doi:10.1016/j.isci.2023.106118

70. Read GH, Bailleul J, Vlashi E, Kesarwala AH. Metabolic response to radiation therapy in cancer. *Mol Carcinog*. 2022;61(2):200-224. doi:10.1002/mc.23379

71. Tang L, Wei F, Wu Y, et al. Role of metabolism in cancer cell radioresistance and radiosensitization methods. *J Exp Clin Cancer Res*. 2018;37(1):87. doi:10.1186/s13046-018-0758-7

72. Gerlinger M, Swanton C. How Darwinian models inform therapeutic failure initiated by clonal heterogeneity in cancer medicine. *Br J Cancer*. 2010;103(8):1139-1143. doi:10.1038/sj.bjc.6605912

73. Kern SE. Why your new cancer biomarker may never work: recurrent patterns and remarkable diversity in biomarker failures. *Cancer Res*. 2012;72(23):6097-6101. doi:10.1158/0008-5472.CAN-12-3232

74. Curtis SB. Lethal and potentially lethal lesions induced by radiation—a unified repair model. *Radiat Res*. 1986;106(2):252-270.

75. Wang Y, Li X, Konanur M, et al. Towards optimal deep fusion of imaging and clinical data via a model-based description of fusion quality. *Med Phys*. 2023;50(6):3526-3537. doi:10.1002/mp.16181

76. Collins GS, Reitsma JB, Altman DG, Moons KG. Transparent reporting of a multivariable prediction model for individual prognosis or diagnosis (TRIPOD): the TRIPOD Statement. *BMC Med*. 2015;13. doi:10.1186/s12916-014-0241-z

77. Abraham A, Pedregosa F, Eickenberg M, et al. Machine learning for neuroimaging with scikit-learn. *Front Neuroinform*. 2014;8:14. doi:10.3389/fninf.2014.00014

78. Parmar C, Grossmann P, Bussink J, Lambin P, Aerts H. Machine learning methods for quantitative radiomic biomarkers. *Sci Rep*. 2015;5:13087. doi:10.1038/srep13087

79. Hou R, Lo JY, Marks JR, Hwang ES, Grimm LJ. Classification performance bias between training and test sets in a limited mammography dataset. *PLoS One*. 2024;19(2):e0282402. doi:10.1371/journal.pone.0282402

80. Chen Y, Yang Z, Zhao J, et al. A radiomics-incorporated deep ensemble learning model for multi-parametric MRI-based glioma segmentation. *Phys Med Biol*. 2023;68(18). doi:10.1088/1361-6560/acf10d

SUPPORTING INFORMATION

Additional supporting information can be found online in the Supporting Information section at the end of this article.

How to cite this article: Stevens JB, Je J, Riley BA, et al. Development and application of a novel tumor habitat analysis technique based on dynamical modeling. *Med Phys*. 2025;52:e18032. https://doi.org/10.1002/mp.18032